Linearized no-slip boundary conditions at a rough surface

Paolo Luchini†

DIIN, Università di Salerno, Italy

Linearized boundary conditions are a commonplace numerical tool in any flow problems where the solid wall is nominally flat but the effects of small waviness or roughness are being investigated. Typical examples are stability problems in the presence of undulated walls or interfaces, and receptivity problems in aerodynamic transition prediction or turbulent flow control. However, to pose such problems properly, solutions in two mathematical distinguished limits have to be considered: a *shallow-roughness* limit, where not only roughness height but also its aspect ratio becomes smaller and smaller, and a *small-roughness* limit, where the size of the roughness tends to zero but its aspect ratio need not. Here a connection between the two solutions is established through an analysis of their far-field behaviour. As a result, the effect of the surface in the small-roughness limit, obtained from a numerical solution of the Stokes problem, can be recast as an equivalent shallow-roughness linearized boundary condition corrected by a suitable *protrusion coefficient* (related to the protrusion height used years ago in the study of riblets) and a *proximity coefficient*, accounting for the interference between multiple protrusions in a periodic array. Numerically computed plots and interpolation formulas of such correction coefficients are provided.

Key words: boundary layers, receptivity, low-Reynolds-number flows

1. Introduction: shallow roughness versus small roughness

In any flow problem where small perturbations to a nearly flat solid wall are being investigated, linearized boundary conditions are the first tool that comes to mind for either analytical or numerical calculations. Examples of the use of such linearized boundary conditions can be found for example in a large literature on interfacial instabilities (e.g. Joseph *et al.* 1997) and in boundary layer receptivity calculations aimed at aerodynamic transition prediction (e.g. Hill 1995).

Typically, if $z = 0$ represents the flat reference surface and $z = \epsilon h(x, y)$ the actual wall, the velocity field $\boldsymbol{v} = (u, v, w)$ is written as a perturbation expansion in ϵ:

$$\boldsymbol{v} = \boldsymbol{v}^{(0)} + \epsilon \boldsymbol{v}^{(1)} + \cdots . \tag{1.1}$$

The exact zero-velocity boundary condition at a solid wall,

$$\boldsymbol{v}[x, y, \epsilon h(x, y)] = 0, \tag{1.2}$$

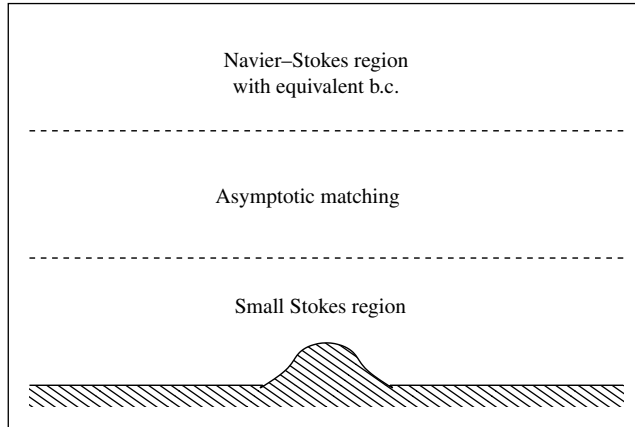† Email address for correspondence: luchini@unisa.it

FIGURE 1. Matched asymptotic expansion.

is replaced by its Taylor expansion in powers of ϵ, the first order of which reads

$$\boldsymbol{v}[x, y, \epsilon h(x, y)] \simeq \epsilon \boldsymbol{v}^{(1)}(x, y, 0) + \epsilon h(x, y) \boldsymbol{v}_z^{(0)}(x, y, 0) = 0. \tag{1.3}$$

Thus the presence of wall corrugations becomes equivalent to a non-zero boundary condition for $\boldsymbol{v}^{(1)}$ assigned at the unperturbed wall.

For definiteness we shall assume that the velocity field obeys the non-dimensional incompressible Navier–Stokes equations

$$\boldsymbol{\nabla} \cdot \boldsymbol{v} = 0, \tag{1.4a}$$

$$\boldsymbol{v}_t + \boldsymbol{v} \cdot \boldsymbol{\nabla} \boldsymbol{v} + \boldsymbol{\nabla} p = \frac{1}{Re} \nabla^2 \boldsymbol{v}, \tag{1.4b}$$

although it should be clear that the boundary conditions (1.2) or (1.3) apply equally well to other problem variations such as boundary layer or local-stability approximations. Even compressibility does not change the picture much, because near the wall the local Mach number will tend to zero with ϵ.

It can be remarked that this standard linearization approach produces no $w^{(1)}$ first-order perturbation to the wall-normal velocity, because the continuity equation (1.4a) entails that $w_z^{(0)}(x, y, 0) = 0$. This is peculiar, as intuitively one might expect the primary effect of the wall modification to be a normal-velocity perturbation, the only one that occurs in inviscid flow. Just as counter-intuitively, if the unperturbed velocity field $\boldsymbol{v}^{(0)}$ is unidirectional (for instance, only has a non-zero $u^{(0)}$ component), no $v^{(1)}(x, y, 0)$ cross-flow perturbation will ever be generated, even by apparently skewed geometries. In addition, no estimate exists to date of the parameter range in which the approximation (1.3) is reliable and these additional velocity components can really be neglected. We shall endeavour in this paper to determine such a parameter range, and also corrections that can be applied to recover accuracy when the range is exceeded to a certain extent.

To this end we shall compare the above to a different approach to the problem, one in which a matched asymptotic expansion is performed. The solution domain is divided into three regions according to figure 1. A solution of the Navier–Stokes (or boundary layer, stability, etc.) problem far from the wall is matched to a solution of the Stokes problem near the wall through a common asymptotic behaviour.
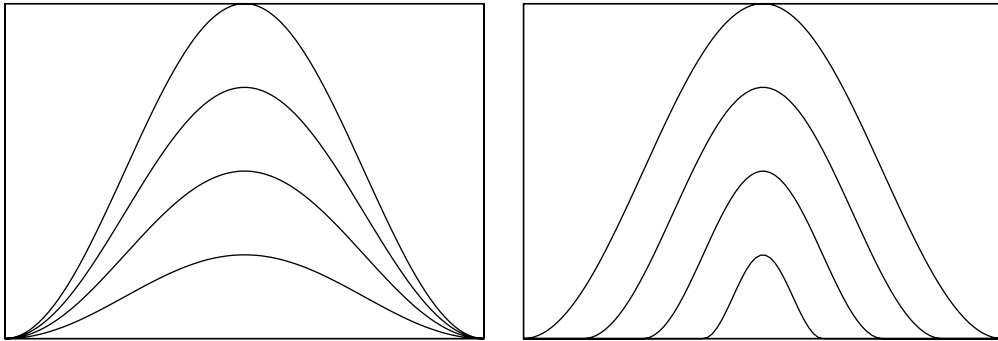
FIGURE 2. Shallow-roughness limit, $z = \epsilon h(x, y)$, versus small-roughness limit, $z = \epsilon h(x/\epsilon, y/\epsilon)$.

Equivalently one could say that the asymptotic far-distance behaviour of the Stokes problem becomes an effective boundary condition for the outer problem.

Examples of this second approach can be found in the calculation of the protrusion-height difference of riblets, which measures their differential action on parallel flow and cross-flow, by Luchini, Manzo & Pozzi (1991), and in Sarkar & Prosperetti (1996), who introduced an effective boundary condition representative of a surface with randomly distributed roughness. Intermediate between the two approaches is the one by Kamrin, Bazant & Stone (2010), who computed the effective slip boundary condition for a periodic surface through a perturbative expansion up to second order in roughness height.

In order to connect and compare these different formulations of approximate wall boundary conditions, we have to carefully consider two mathematical distinguished limits (see figure 2). In the first limit, which we shall name the *shallow-roughness* limit, a family of surfaces is involved, defined as $z = \epsilon h(x, y)$, that become smoother and smoother (of smaller and smaller slope) as $\epsilon \to 0$. On the other hand the second limit, which we shall name the *small-roughness* limit, is concerned with a family of surfaces defined as $z = \epsilon h(x/\epsilon, y/\epsilon)$, which remain geometrically similar to themselves (in particular, retain their slope) when $\epsilon \to 0$.

The differential equations (but not the boundary conditions) governing either limit are linear. Once ϵ is small enough, flow around either a *shallow* or a *small* protuberance will be governed by the Stokes equations

$$\nabla \cdot \boldsymbol{v} = 0, \tag{1.5a}$$

$$\nabla P = \nabla^2 \boldsymbol{v} \tag{1.5b}$$

(where $P = Re\, p$). However, a proper solution of the small-roughness perturbation problem requires actually integrating (1.5) with the exact boundary condition (1.2) (which depends nonlinearly on h) and then extracting the behaviour at infinity of this solution, to be matched to an outer velocity field in the form of an equivalent boundary condition at the surface. Since, as will be seen, the leading behaviour at infinity of the small-roughness problem turns out to bear the same form as the impulse response of the shallow-roughness problem, the two results can be directly compared. For example, it will be confirmed that no equivalent wall-normal $w^{(1)}$ is generated in either case, whereas a *small* skewed fin can generate an equivalent sideways $v^{(1)}$ even though a *shallow* one cannot.

In this paper numerical solutions will be exhibited for a number of shapes, producing in particular the *protrusion coefficient*, which must be applied to the shallow-roughness boundary condition in order to mimic the results of the small-roughness limit. A plot of this coefficient as a function of the aspect ratio enables us to judge whether the shallow-roughness linearized boundary condition is or is not appropriate for a given application, and to correct it when it is not. In addition, a *proximity coefficient* will be introduced to account for the mutual interference of multiple wall perturbations placed in a periodic array.

2. Solution of the shallow-roughness problem

2.1. *Impulse response*

The linearized boundary condition (1.3) effectively transforms the geometrical perturbation of the boundary into a velocity perturbation applied at the unperturbed boundary. Since the problem formed by the Stokes equations (1.5) with such boundary conditions is linear, its solution can be expressed as a superposition of impulse responses.

The half-space velocity impulse response of the Stokes problem is by definition a second-order tensor $\boldsymbol{H}$ such that

$$\boldsymbol{v}(\boldsymbol{x}) = \int_{\xi_3=0} \boldsymbol{H}(\boldsymbol{x} - \boldsymbol{\xi}) \cdot \boldsymbol{v}(\boldsymbol{\xi}) \, \mathrm{d}\xi_1 \, \mathrm{d}\xi_2 \tag{2.1}$$

(notice that only velocity and no pressure appears in this formula).

Equation (2.1) is similar to the double-layer potential used in boundary element methods (e.g. Pozrikidis 1992). The expression of $\boldsymbol{H}$ may be obtained in a number of ways or just verified *a posteriori*, and is equal to twice the normal component of a third-order tensor which Batchelor (1970), for a different application involving stress in a suspension, named a *stresslet*. Namely

$$\boldsymbol{H} = \frac{3}{2\pi} \frac{\boldsymbol{r}\boldsymbol{r}z}{r^5}, \tag{2.2}$$

where $\boldsymbol{r} = \boldsymbol{x} - \boldsymbol{\xi}$ and the juxtaposition $\boldsymbol{r}\boldsymbol{r}$ denotes a dyadic product (whereas a dot, as in (2.1), denotes a contraction). In components (with $i, j, k = 1 \ldots 3$; $x_1 = x$, $x_2 = y$, $x_3 = z$; and implied summation on the repeated index):

$$H_{ij} = \frac{3}{2\pi} \frac{(x_i - \xi_i)(x_j - \xi_j)x_3}{[(x_k - \xi_k)(x_k - \xi_k)]^{5/2}}. \tag{2.3}$$

That (2.3) is the impulse response of this problem is easily verified as follows: (i) it is a solution of the Stokes equations; (ii) all three components of velocity vanish for $x_3 = 0$ and $(r_1, r_2) \neq (0, 0)$; and (iii) $\int H_{ij} \, \mathrm{d}r_1 \, \mathrm{d}r_2 = \delta_{ij} \, \forall x_3$, which implies that H_{ij} tends to a Dirac δ function when $x_3 \to 0$. Equation (2.3) may also be seen as a limiting case of the Stokes flow induced by a particle moving near a plane wall (Blake 1971), but Blake's formula involves additional terms and complications which do not appear in the limit.

A stresslet is the symmetrized gradient of a *Stokeslet* $\boldsymbol{S}$, the free-space Green's function of the Stokes problem, namely

$$\boldsymbol{S} = \frac{1}{8\pi} \frac{\boldsymbol{r}\boldsymbol{r} + r^2 \boldsymbol{I}}{r^3}, \tag{2.4}$$

the latter providing the response to a unit impulsive force (as opposed to a velocity).

It is worth emphasizing that the Stokes flow generated by a protuberance sitting on the boundary and the Stokes flow past an isolated obstacle in free space, the far field of one being represented by (2.2) and the far field of the other by (2.4), have substantially different behaviour. Indeed, **S** is $O(r^{-1})$ at infinity and transports a finite rate of momentum, whereas **H** is $O(r^{-2})$ and its momentum transport at infinity is zero. This mathematical difference reflects the physical difference that whereas in free space the reaction to the force exerted on a particle cannot be borne other than by the virtual boundary at infinity, in the presence of an infinite solid wall the reaction force generated by an obstacle is discharged on the remainder of the wall itself.

Yet another difference between (2.2) and (2.4) is that whereas **S** produces a zero net mass flow rate, some components of **H** have non-zero mass flow rate at infinity. This fact will have important consequences in the following sections.

2.2. *Asymptotic behaviour*

The behaviour of the velocity field (2.1) at a large distance from its source can be obtained, just as in the analogous problem for the Laplace equation, by expanding $H(x - \xi)$ in the form of a Taylor series in ξ and reinterpreting the result as a sum of multipole fields. This Taylor series is

$$v(x) = \sum_{m=0}^{\infty} \sum_{n=0}^{m} \frac{(-1)^m}{(m-n)!\, n!} \frac{\partial^m H}{\partial x_1^{m-n} \partial x_2^n} \cdot \int_{\xi_3=0} \xi_1^{m-n} \xi_2^n v(\xi) \, d\xi_1 \, d\xi_2. \tag{2.5}$$

As **H** is a homogeneous function in accordance with the scale invariance of the Stokes problem, in particular one proportional to r^{-2}, every derivative of order m in (2.5) is in turn a homogeneous function $O(r^{-m-2})$. Therefore, the Taylor series (2.5) doubles up as an ordered series of integer powers of r^{-1}. Its leading term at infinity is simply

$$v(x) \simeq H(x) \cdot \int_{\xi_3=0} v(\xi) \, d\xi_1 \, d\xi_2, \tag{2.6}$$

and is $O(r^{-2})$ provided that the boundary velocity has non-zero integral.

For an unperturbed velocity field characterized by a unit velocity gradient directed in the x direction, $u^{(0)} = z$, the order-one boundary condition (1.3) reads

$$u^{(1)}(x_1, x_2, 0) = -h(x_1, x_2), \quad v^{(1)}(x_1, x_2, 0) = 0, \quad w^{(1)}(x_1, x_2, 0) = 0, \tag{2.7}$$

and therefore (2.6) further specializes to

$$v_i^{(1)}(x) \simeq -H_{i1}(x) \int h(\xi_1, \xi_2) \, d\xi_1 \, d\xi_2 \quad \text{as } r \to \infty. \tag{2.8}$$

A three-dimensional rendering of the vector field $H_{i1}(x)$ is provided in figure 3. As may be easily deduced from (2.2), the velocity vector is everywhere in the radial direction, and oriented towards the wall protuberance in one quadrant and outwards from it in the other.

3. The small-roughness limit

3.1. *Position of the problem*

We now move on to examining the small-roughness limit, the one in which the wall shape is assumed to belong to a family of surfaces of the form $z = \epsilon h(x/\epsilon, y/\epsilon)$. If the coordinates are rescaled as $x' = x/\epsilon$, $y' = y/\epsilon$ and $z' = z/\epsilon$, and at the same time velocity is also rescaled by a factor of ϵ so as to keep the velocity gradient
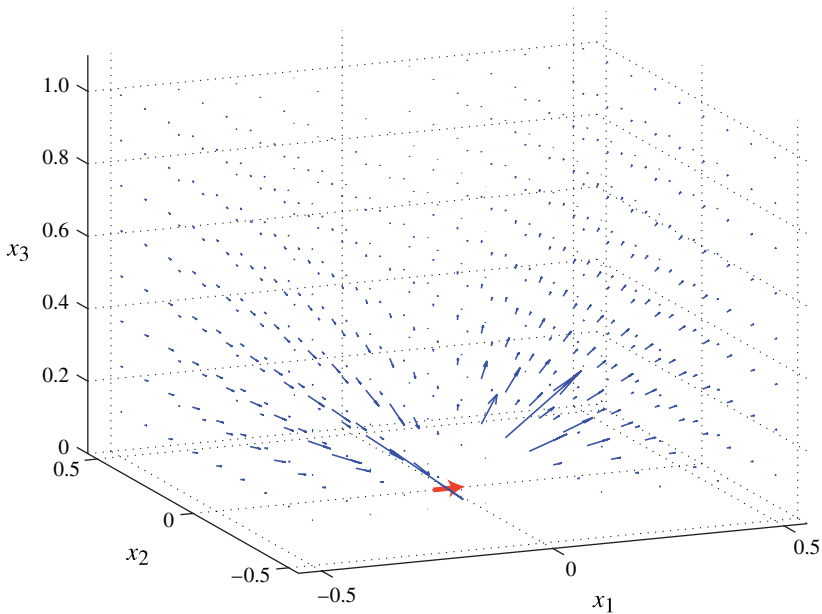
FIGURE 3. (Colour online) Three-dimensional plot of the response to an impulsive boundary velocity.

unchanged, the Navier–Stokes equations (1.4) retain exactly the same form except that the Reynolds number becomes $Re' = \epsilon^2 Re$. In this distinguished limit, the leading term of their perturbative expansion in ϵ is represented by the solution of the Stokes equations (1.5) about the fixed geometry $z' = h(x', y')$, which can be obtained independently of ϵ by numerical means.

The boundary conditions for this Stokes problem are $v = 0$ at the wall and an imposed velocity gradient at infinity (to be matched to the velocity gradient at the wall of the outer region of figure 1). Since the problem is linear in this velocity gradient (even though not in h), we may assume that the velocity gradient is unitary and oriented in the x direction.

In order to make our results directly comparable to those of the shallow-roughness limit, we may also subtract the unperturbed velocity field $u = z$ (itself an exact solution of the Stokes equations), and introduce the induced velocity v' such that

$$u' = u - z, \quad v' = v, \quad w' = w. \tag{3.1}$$

In this equivalent problem, homogeneous conditions are imposed at infinity and the u' component of velocity at the physical boundary equals $-z'$. In components:

$$u'[x', y', h(x', y')] = -h(x', y'), \quad v'[x', y', h(x', y')] = 0, \quad w'[x', y', h(x', y')] = 0. \tag{3.2}$$

It may be noticed that these boundary conditions for v' closely resemble the boundary conditions (2.7) for $v^{(1)}$, except that all three are imposed at the height h rather than at the height 0.

3.2. *Asymptotic behaviour*

The asymptotic behaviour at infinity of the induced velocity field can classically be established through an analysis of separable solutions in spherical coordinates. Owing to the scale invariance of the Stokes problem, these solutions may be expected to be of the form $r^{-\alpha}F(\theta, \phi)$, where θ and ϕ are spherical angles, for suitable eigenvalues of the exponent α such that a non-trivial F exists satisfying homogeneous boundary conditions at the equatorial plane. In the analogous derivation for the Laplace equation, similarly defined eigenfunctions are known as spherical harmonics. The eigenfunctions we need are the equivalent of spherical harmonics for the Stokes problem.

In fact we can avoid a somewhat cumbersome calculation, and in the process recognize that the eigenvalues of α must be integer numbers, if we observe that the exact same eigenfunctions govern the asymptotic behaviour of the solution of the shallow-roughness problem. The non-homogeneous boundary conditions at the modified bounded portion of the surface, whether they are of the form (2.7) or of the form (3.2), determine only the coefficients of the eigenfunctions and not their expression. Since we already know the asymptotic expansion (2.5) for the shallow-roughness problem, we can expect the far-field behaviour in the small-roughness limit to be represented by a similar series, namely

$$\boldsymbol{v}'(\boldsymbol{x}') = \sum_{m=0}^{\infty} \sum_{n=0}^{m} \frac{(-1)^m}{(m-n)!\, n!} \frac{\partial^m \boldsymbol{H}}{\partial x_1'^{m-n} \partial x_2'^n} \cdot \boldsymbol{q}_{mn}, \tag{3.3}$$

the only difference being that $\boldsymbol{q}_{mn}$ are now unknown vector coefficients.

The leading term of (3.3) is

$$\boldsymbol{v}'(\boldsymbol{x}') \simeq \boldsymbol{H}(\boldsymbol{x}') \cdot \boldsymbol{s} \quad \text{as } r \to \infty, \tag{3.4}$$

where the coefficient $\boldsymbol{s} \equiv \boldsymbol{q}_{00}$ is a constant vector. Again, the only difference between (2.8) and (3.4) is that for a *shallow* perturbation $\boldsymbol{s}$ has a closed-form explicit expression whereas for a *small* one it does not. It follows that the s_2 and s_3 components are no longer bound to be zero when the unperturbed flow is aligned with the x_1 direction; in general the $\boldsymbol{s}$ vector is no longer obliged to be parallel to the unperturbed flow. Nonetheless its wall-normal component, s_3, can be immediately obtained from mass conservation, because H_{33} is the only component of $\boldsymbol{H}$ to produce a non-zero total mass flow rate at infinity, which must equal the total mass flow rate at the wall. It thus follows that for an impermeable solid boundary of any shape s_3 is zero, and the H_{i3} components do not participate in the far-field velocity.

It was observed in connection with the shallow-roughness problem (1.3) that no normal velocity $w^{(1)}$ is produced, and therefore H_{i3} does not participate in its asymptotic solution. We now see that this remains true in general, and only s_1 and s_2 are left to be determined in the next sections.

4. Protrusion coefficients and effective boundary condition

Once it has been established that a *small* wall perturbation produces the same effect, insofar as its asymptotic velocity field is concerned, as a *shallow* one characterized by a suitable wall velocity, it becomes natural to normalize the coefficients s_1 and s_2, which can be extracted from a numerical solution of the Stokes equations, to the value of s_1 that would be obtained in the shallow-roughness case. The latter, for a unit velocity gradient $u_z^{(0)} = 1$ oriented in the x direction, is simply the negative volume of

the wall perturbation:

$$s_1 = - \int h(x, y) \, dx \, dy \equiv -V. \tag{4.1}$$

We are thus led to define non-dimensional *protrusion coefficients* $c_{11} \equiv -s_1/V$ and $c_{21} \equiv -s_2/V$, expected to be such that $c_{11} \to 1$ and $c_{21} \to 0$ as the protrusion's aspect ratio tends to zero. If the protrusion coefficients of a given geometry are known, the matching depicted in figure 1 can be carried out by simply multiplying h with the corresponding protrusion coefficients in the linearized boundary condition (1.3):

$$u^{(1)}(x, y, 0) = -c_{11}h(x, y)u_z^{(0)}, \quad v^{(1)}(x, y, 0) = -c_{21}h(x, y)u_z^{(0)}, \quad w^{(1)}(x, y, 0) = 0. \tag{4.2}$$

Conversely, the adequacy of the standard linearized boundary condition (1.3) can be judged by looking at the difference between the numerically computed protrusion coefficients and $(1, 0)$.

Since the dependence of the solution of the Stokes equations on the external velocity gradient is linear (although its dependence on $h(x, y)$ is not), (4.2) can be completed to account for an arbitrary direction of the external velocity gradient once protrusion coefficients are computed in two orthogonal directions. Equation (4.2) then becomes

$$v_i^{(1)}(x_1, x_2, 0) = -c_{ij}h(x_1, x_2)v_{j,z}^{(0)}, \quad v_3^{(1)}(x_1, x_2, 0) = 0 \tag{4.3}$$

where $i, j = 1 \ldots 2$ (subscript $, z$ instead representing a derivative) and the four protrusion coefficients c_{ij} transform geometrically like a two-dimensional tensor.

5. Relation to past studies of periodic arrangements

Past studies of Stokes flow near perturbed boundaries have mostly dealt with periodic arrays or statistically homogeneous random arrangements of protuberances. In order to relate to such studies, we must first connect the protrusion coefficients of an isolated protuberance to those of a periodic array.

For an isolated protrusion, the velocity far field is proportional to **H** and, according to (3.3), approaches its behaviour at infinity rather slowly with a relative error $O(1/r)$. For a periodic array of equal shapes, instead, the behaviour at infinity of the Stokes solution is expressed by a Fourier series, all of whose terms except the first decay exponentially with z. More precisely, the zero-wavenumber Fourier component of the solution of the Stokes equations (1.5) is constant with z (everywhere, and thus also asymptotically), implying that the induced velocity u' tends to a constant u'_∞ and that

$$u'_\infty = \frac{1}{A} \int u(x, y, 0) \, dx \, dy = -\frac{1}{A} \int h(x, y) \, dx \, dy = -\bar{h} \tag{5.1}$$

in the shallow-roughness limit, or $u'_\infty = -c_{11}\bar{h}$ in the small-roughness limit, where A denotes the area of a fundamental cell of the periodic arrangement (or average area per protuberance of the random arrangement) and therefore $\bar{h}$ denotes its mean height.

Periodic arrangements of protrusions were studied in the past by Bechert & Bartenwerfer (1989) (for the longitudinal two-dimensional viscous flow, governed by the Laplace equation), Luchini *et al.* (1991) (for the transverse two-dimensional Stokes flow), Sarkar & Prosperetti (1995) (for the Laplace equation in a three-dimensional setting), Sarkar & Prosperetti (1996) (who formulated the general problem of Stokes flow past a periodic or random array of protuberances, and solved it analytically for sparse hemispherical bosses) and Kamrin *et al.* (2010) (who calculated the second order of the shallow-roughness perturbative expansion in ϵ). Bechert & Bartenwerfer

(1989) and Luchini *et al.* (1991) used the name longitudinal and transverse *protrusion heights* for what are here the quantities $c_{11}\bar{h}$ and $c_{22}\bar{h}$ (c_{21} and c_{12} being zero in the two-dimensional problem), because the asymptotic velocity profiles $v_i \simeq (z - c_{ii}\bar{h})v_{i,z}^{(0)}$ appear each to originate at the height $c_{ii}\bar{h}$ (no summation implied). Kamrin *et al.* (2010) adopted the name of *mobility tensor* for the protrusion-height tensor $c_{ij}\bar{h}$, and provided an explicitly symmetric second-order approximation of this tensor in terms of the Fourier components of $h(x, y)$, a numerical example of which will be given in § 8. In fact Sarkar & Prosperetti (1996) had already proved that, as a consequence of the Stokes problem's reciprocity properties, the exact c_{ij} tensor must also be symmetric. An alternative proof of this symmetry is given in the Appendix.

Sarkar & Prosperetti (1996) used the symbol $1 + k$ for the coefficient that is c_{11} here, and calculated a value of 1.3156 for it in the example of sparse hemispherical bosses. However, according to Sarkar & Prosperetti (private communication), a missing factor of π was later found in these calculations by Mauro Sbragaglia, while working with Prosperetti on a related problem. With this error corrected the coefficient $1 + k$ becomes 4.1331, perfectly reproduced by the present computations as reported in figure 5 below. This protrusion coefficient is larger than the corresponding coefficient for the Laplace equation, calculated to be 3 by Sarkar & Prosperetti (1995); it is proved in the Appendix that a similar inequality must hold in general.

6. Numerical computation

Numerical protrusion coefficients for a few common shapes have been obtained from a multigrid finite-difference Stokes solver on a staggered square grid, with the wall represented as an immersed boundary, and periodic boundary conditions in the homogeneous directions. From a computational viewpoint a periodic array, in addition to being convenient to implement through periodic boundary conditions, allows the height of the computational domain to be not very large owing to exponential convergence of the induced velocity field. On the other hand, because of the nonlinear dependence of (3.2) on h, a periodic arrangement of equal shapes will not have exactly the same protrusion coefficient as an isolated one; the period has to be chosen by trial and error to be large enough that the behaviour of an isolated roughness element is approximated with sufficient accuracy. Conversely, if a square lattice is considered with both periods equal to 1, as will be assumed in what follows, the volume of the chosen protrusion has to be sufficiently small. As long as the array is sparse enough that the numerical computation on a periodic domain approximates the behaviour of an isolated protuberance, s_1 and s_2 in (3.4) are approximated by u'_∞ and v'_∞ respectively, and the protrusion coefficients can be calculated as

$$c_{11} = -u'_\infty/V, \quad c_{21} = -v'_\infty/V. \tag{6.1}$$

A number of different geometrical shapes have been studied numerically, each one for a range of aspect ratios. Assuming a period of 1 in both the x and y directions, numerical parameters are the grid size, the height of the discretization domain and the size (diameter) of the protuberance. A grid-convergence study of our immersed-boundary discretization is reported in figure 4 for two typical shapes. Convergence with respect to the height of the domain is exponentially fast: a height of $z = 1$ proved sufficient to obtain a less than 10^{-4} error in most cases. The effect of roughness size on accuracy will be discussed in § 9.
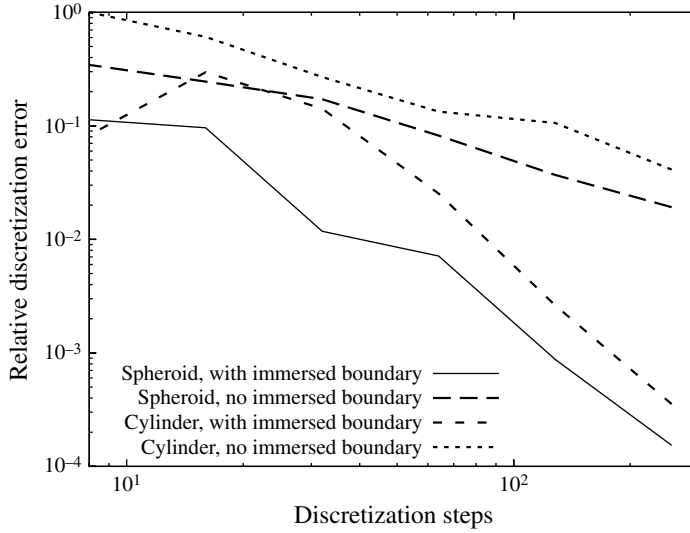
FIGURE 4. Error in the protrusion coefficient versus number of discretization steps in a period.

Cylinder	if $x^2 + y^2 < R^2$ then $z < a$ else $z < 0$
Smoothed cylinder	$z < \dfrac{a}{1 + \exp\left[10\left(\sqrt{x^2 + y^2}/R - 1\right)\right]}$
Square cylinder	if $|x| < R$ and $|y| < R$ then $z < a$ else $z < 0$
Cone	if $x^2 + y^2 < R^2$ then $z < a(1 - \sqrt{x^2 + y^2}/R)$ else $z < 0$
Gaussian	$z < a \exp[-(x^2 + y^2)/(4R^2)]$
Spheroid	if $x^2 + y^2 < R^2$ then $z < a\sqrt{1 - (x^2 + y^2)/R^2}$ else $z < 0$
3:1 ellipsoid	if $(3x/R)^2 + (y/R)^2 < 1$ then $z < a\sqrt{1 - (3x/R)^2 - (y/R)^2}$ else $z < 0$

TABLE 1. List of wall shapes used in the computation, parametrized by their (positive or negative) height a and radius R, each one specified through the logical expression used by the computer program to test whether a point of coordinates x, y, z falls in its interior.

7. Numerical results

7.1. *Axisymmetric bumps*

Figure 5 shows the computed protrusion coefficient as a function of the aspect ratio for a number of axisymmetric geometrical shapes as described in table 1.

The square cylinder is included here because, as will be seen in § 7.3, it also behaves like an axisymmetric shape in that it produces the same asymptotic velocity field independently of its orientation.

The quantitative definition of the aspect ratio is to some extent arbitrary, but it affects whether the curves in figure 5 fall more or less near to each other. After defining the aspect ratio of the cylinder as the ratio of its height to diameter, a reasonably good collapse of other shapes' data on the cylinder's curve has been obtained by defining their aspect ratio as the aspect ratio of the cylinder that would
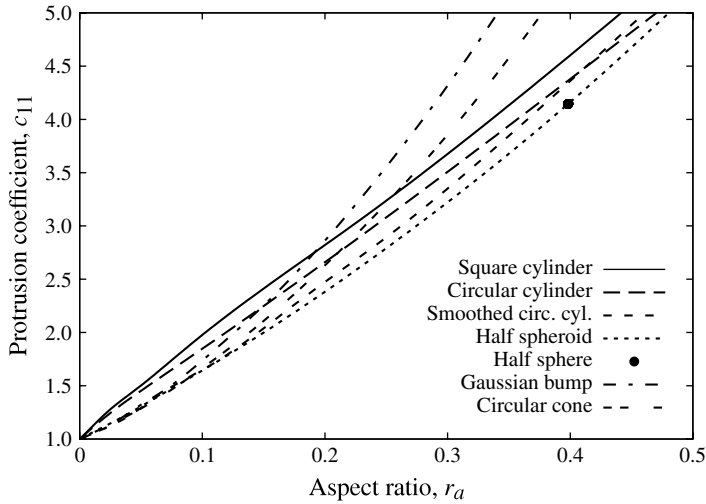
FIGURE 5. Protrusion coefficient for axisymmetric bumps. For the circular cylinder, $r_a =$ height/diameter. Other shapes have the aspect ratio of the circular cylinder with the same barycentre and volume.

have the same barycentre and volume. As can be seen, with this definition the different curves fall fairly close to each other up to an aspect ratio of 0.2, and for the bluffer shapes (i.e. with the exception of the cone and Gaussian) up to 0.5, so that a common trend can be recognized for all the shapes involved. In fact this trend is not far from a straight line, a fact which makes the protrusion coefficient fairly simple to predict in this range of aspect ratios, where it is nonetheless non-trivially larger than unity.

7.2. *Cavities*

Nothing in the previous analysis prevents the height of the protrusion from becoming negative, i.e. the protrusion from transforming into a cavity. A plot of the protrusion coefficient for cavities is reported in figure 6.

It may be observed that in the case of cavities the linearized boundary condition (2.7) overestimates the induced velocity, i.e. the protrusion coefficient is smaller than unity. An interesting trend is observed if its reciprocal $1/c_{11}$ is plotted (see figure 7): all the curves tend to straight lines at large negative aspect ratios, but this time with visibly different slopes. A simple interpretation of this behaviour emerges if one observes that the volume of the cavity divided by its aspect ratio tends to be proportional to the area of the cavity planform; therefore a protrusion coefficient inversely proportional to the aspect ratio is a sign that the induced velocity of the cavity tends to a constant for large depth and in this limit depends on its area only.

7.3. *Skewed shapes*

As noted in §1, the induced velocity field is always aligned with the inducing velocity in the shallow-roughness limit, even when a skewed geometry (such as a slanted winglet) would let us predict the presence of a sideways component. Therefore we expect the c_{21} protrusion coefficient, which is allowed to be non-null in the small-roughness limit, to tend to zero with decreasing aspect ratio. This is indeed the case, as shown in figure 8 for the example of an ellipsoidal shape.
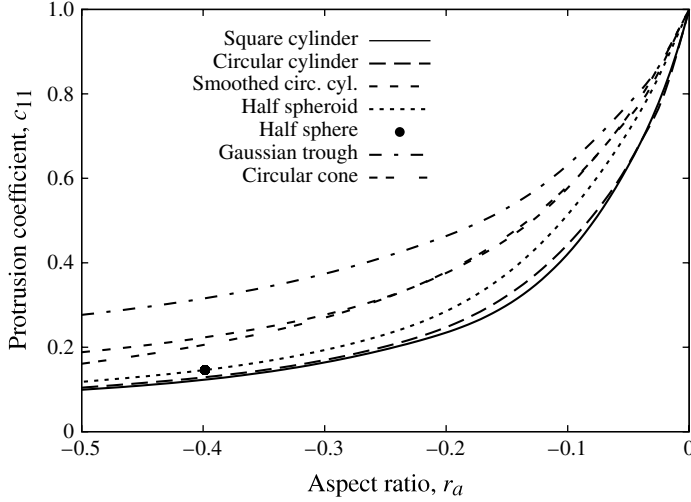
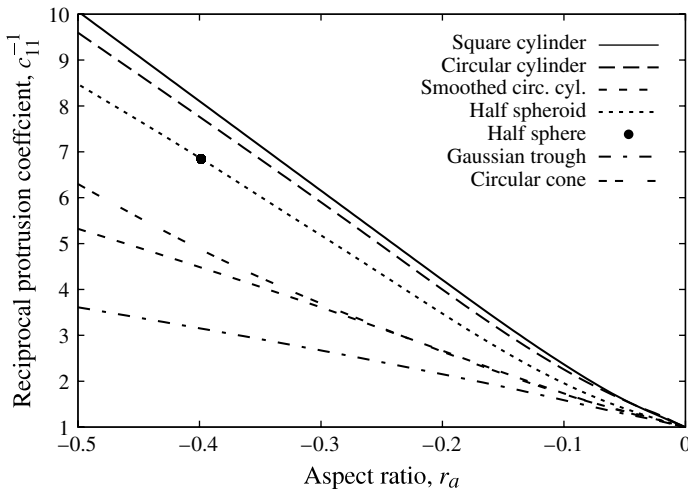FIGURE 6. Protrusion coefficient for axisymmetric cavities.

FIGURE 7. Protrusion coefficient of cavities on a reciprocal scale.

More specifically, one can remark that since the c_{ij} protrusion coefficients form a symmetric 2×2 tensor, this tensor becomes diagonal in two orthogonal principal directions: its cross-flow component c_{21} ($=c_{12}$) is zero when the main velocity comes from one of these directions, and always attains its maximum at $45°$ with respect to the principal directions. In the example of the ellipsoid these are obviously the directions of its symmetry axes, but they remain orthogonal even for arbitrary and less symmetrical shapes. The two principal values have the same role as the longitudinal and transverse *protrusion heights*, as defined for drag-reducing riblets by Bechert & Bartenwerfer (1989) and Luchini *et al.* (1991). The principal values coincide, and c_{21} becomes identically zero in any orientation, if the geometrical shape of the protuberance has higher than C_2 rotational symmetry (transforms into itself under a
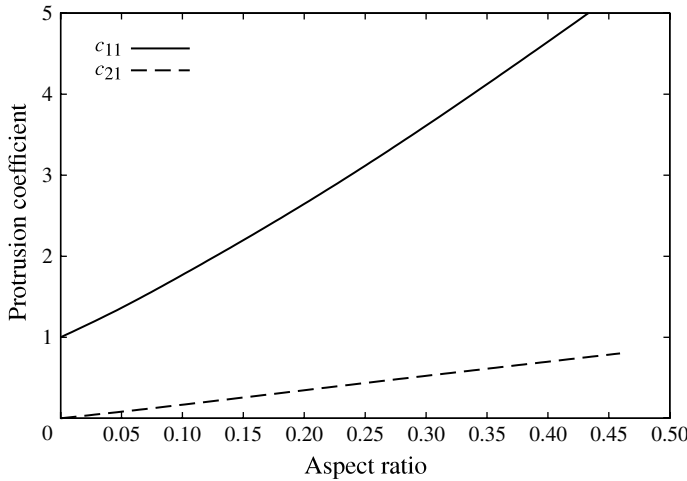
FIGURE 8. Longitudinal and cross-flow protrusion coefficients for a 45°-slanted 3:1 ellipsoid.

rotation of less than 180°). For a square or an equilateral triangle, for instance, the orientation of the main stream is totally irrelevant and the induced velocity remains parallel to the base flow velocity just as though they were axisymmetric shapes.

8. Approximations of the protrusion coefficient and their applicability limits

Although the reported values of the protrusion coefficient are a numerical result and do not have an analytic expression, their relatively smooth behaviour makes a fit possible by simple interpolation formulas. As an example, one simple function of the aspect ratio r_a that behaves linearly for $r_a \to +\infty$, proportionally to $1/r_a$ for $r_a \to -\infty$, and equals 1 for $r_a = 0$ can be obtained from the solution formula of quadratic equations:

$$c_p = 5.2\, r_a + \sqrt{1 + (5.2\, r_a)^2}. \tag{8.1}$$

Figure 9 reproposes the protrusion coefficient of a smoothed circular cylinder, over a range encompassing positive and negative values of the aspect ratio, in comparison with (8.1). As may be seen, the fit is satisfactory for all practical purposes. The same figure also reports the prediction of the shallow-roughness limit, which is a protrusion coefficient constantly equal to 1, and the prediction for the same geometry of the second-order approximation of Kamrin *et al.* (2010), which is a straight line tangent to the exact curve at the origin (with a slope of 5.568 calculated from their equation (3.4)). The application range of the standard shallow-roughness boundary condition (1.3), the estimation of which was one of the purposes of this paper, is clearly the one where the protrusion coefficient departs from 1 less than the allowed error. For instance, for a maximum error of the order of 10–11 % the aspect ratio must be contained within ±0.02 (or ±0.002 for 1 %), and this range can be expected to be qualitatively valid for other wall shapes as well. By a similar argument, the Kamrin *et al.* (2010) approximation may be estimated to be valid (within a 10 % error) for an aspect ratio in the [−0.07, +0.10] interval.
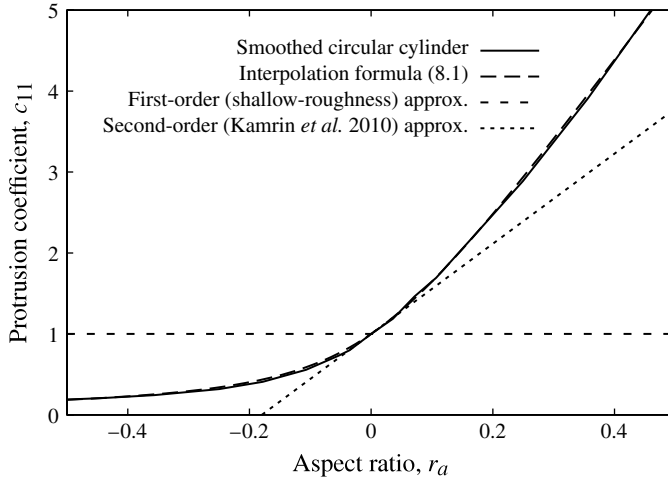
FIGURE 9. Comparison of the numerical result with its various approximations.

9. Proximity interaction

Let us now return to the relationship between the effects of an isolated wall irregularity and of a periodic arrangement of them. In the shallow-roughness limit there is no difference, because the effects of multiple wall irregularities superpose linearly. For a periodic arrangement of equal shapes, (2.1) may be rewritten as

$$v(x) = \sum_{i=-\infty}^{\infty} \sum_{j=-\infty}^{\infty} \int_{e_1 \otimes e_2} H(x - \xi - ie_1 - je_2) \cdot v(\xi)\, \mathrm{d}S, \qquad (9.1)$$

where e_1 and e_1 are the two fundamental periods and $e_1 \otimes e_2$ is the elementary parallelogram of the periodic arrangement. For the square pattern used in the present numerical computations, where e_1 and e_2 are unitary and mutually orthogonal and coincide with the x and y unit vectors of the reference frame, and with $v(\xi)$ given in the shallow-roughness limit by (2.7), the induced velocity u' calculated from (9.1) turns out to be

$$u'(x, y, z) = -\sum_{i=-\infty}^{\infty} \sum_{j=-\infty}^{\infty} \int_0^1 \int_0^1 h(\xi, \eta)$$

$$\times \frac{3}{2\pi} \frac{(x - \xi - i)^2 z}{[(x - \xi - i)^2 + (y - \eta - j)^2 + z^2]^{5/2}}\, \mathrm{d}\xi\, \mathrm{d}\eta. \qquad (9.2)$$

Its limit when h tends to be proportional to a δ function (i.e. when the diameter of the protuberance becomes negligible compared to the period, in the present normalization where the period is the reference length) is given by

$$u'(x, y, z) \simeq -V \sum_{i=-\infty}^{\infty} \sum_{j=-\infty}^{\infty} \frac{3}{2\pi} \frac{(x - i)^2 z}{[(x - i)^2 + (y - j)^2 + z^2]^{5/2}}, \qquad (9.3)$$

with volume $V = \int h(\xi, \eta) \, d\xi \, d\eta$. By comparison with (5.1) we may deduce that

$$\lim_{z \to \infty} \sum_{i=-\infty}^{\infty} \sum_{j=-\infty}^{\infty} \frac{3}{2\pi} \frac{i^2 z}{(i^2 + j^2 + z^2)^{5/2}} = 1, \tag{9.4}$$

and indeed this non-trivial equality is numerically verified.

Let us now see how the picture changes in the small-roughness limit. The relevant boundary condition (3.2) is nonlinear in h and the different protuberances interact; the compound u'_∞ may differ from the sum of their individual contributions. For a general unperturbed velocity gradient $u_z^{(0)}$ the latter would be

$$u'(\boldsymbol{x}) \simeq -c_{11} u_z^{(0)} V \sum_{i=-\infty}^{\infty} \sum_{j=-\infty}^{\infty} \frac{3}{2\pi} \frac{(x-i)^2 z}{[(x-i)^2 + (y-j)^2 + z^2]^{5/2}}, \tag{9.5}$$

which reduces to $u'_\infty = -c_{11} u_z^{(0)} V$ for $z \to \infty$ in accordance with (9.4).

Equation (9.5) in fact becomes valid when $c_{11}V$ is small (but notice that c_{11} itself need not be small); more generally it represents the first term of an expansion of the velocity perturbation in powers of $c_{11}V$. This type of problem belongs in the theory of multiple scattering, as observed by Sarkar & Prosperetti (1996). The next term of the series may be determined in a general way if one observes that when, with growing h, the interaction begins to be significant, the periodic protuberances can still be considered to sit in the far field of one another. Therefore it appears that a better approximation of $u'(\boldsymbol{x})$ than (9.5) is

$$u'(\boldsymbol{x}) \simeq -c_{11}[u_z^{(0)} + u_z'(0)]V \sum_{i=-\infty}^{\infty} \sum_{j=-\infty}^{\infty} \frac{3}{2\pi} \frac{(x-i)^2 z}{[(x-i)^2 + (y-j)^2 + z^2]^{5/2}}, \tag{9.6}$$

where $u_z'(0)$ is the velocity gradient induced at the position of a single protuberance by all the others except itself. Differentiating (9.6) and then letting $\boldsymbol{x} = 0$ gives

$$u_z'(0) = -c_{11} V [u_z^{(0)} + u_z'(0)] S, \tag{9.7}$$

where the interaction constant S is given by

$$S = \sum_{(i,j) \neq (0,0)} \frac{3}{2\pi} \frac{i^2}{(i^2 + j^2)^{5/2}} \simeq 2.1566. \tag{9.8}$$

At the same time the far-field induced velocity becomes

$$u'_\infty = -c_{11} V [u_z^{(0)} + u_z'(0)]. \tag{9.9}$$

Eliminating $u_z'(0)$ between (9.7) and (9.9) yields

$$u'_\infty = -u_z^{(0)} c_{11} V / (1 + S c_{11} V) \tag{9.10}$$

and its inverse

$$c_{11} V = -u'_\infty / (u_z^{(0)} + S u'_\infty). \tag{9.11}$$

Equation (9.10) is the result we are after: it provides the nonlinear proximity correction to the expression (9.5) of the far-field velocity, and may be rewritten as $u'_\infty = -c_p c_{11} u_z^{(0)} V$, where

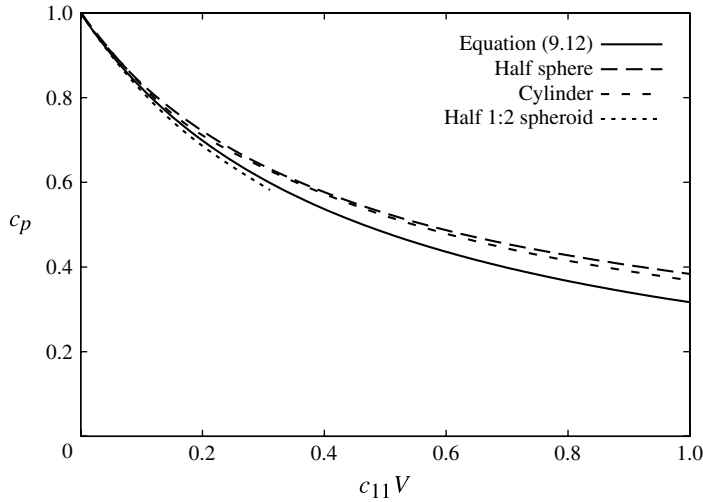$$c_p = (1 + S c_{11} V)^{-1} \tag{9.12}$$

FIGURE 10. Proximity coefficient of (9.12) compared to numerical results for a cylinder of aspect ratio 0.5, a half sphere (aspect ratio 0.398) and a half 1:2 prolate spheroid (aspect ratio 0.199).

is a *proximity* coefficient. (In a dimensional setting, V in this formula must be read as the volume of the protuberance divided by the period cubed.) The dependence of c_p on $c_{11}V$ is universal within the limits of this approximation, and only contains the interaction constant S which depends on the periodic lattice (e.g. it equals 2.1566 for a square array, or 2.2813 for a closely packed hexagonal arrangement) but not on the shape of the protuberance. This is brought out in figure 10, which compares the universal approximation (9.12) with the exact c_p obtained from numerical solutions with three protrusions of different shape and size. It must be noted that the horizontal range of each plot extends up to a diameter such that the protuberances nearly touch each other; the different curves, in addition to having the same tangent at 0 as expected, remain in fairly good agreement over the whole range. (A similar, numerically computed, curve for the Laplace equation is in figure 6 of Sarkar & Prosperetti (1995).)

The inverse relation (9.11) is useful in order to extrapolate the values of c_{11} numerically obtained for non-zero V to their limit for $V \to 0$, something which was actually done for the purpose of producing figures 5–8 and verifying their accuracy.

10. Conclusions

The flow perturbation induced by the linearized boundary condition for a *shallow* wall corrugation, and the full Stokes solution for a *small* one, share a common asymptotic behaviour at large distance. Investigation of this behaviour has enabled us to both establish the operational limits of the linearized boundary condition, i.e. the range of aspect ratio in which it is expected to yield a reasonably good approximation (for instance, for an error of 10 % the aspect ratio must stay within ± 0.02), and extend this range with the aid of correction coefficients.

A peculiarity of the solution obtained from the linearized boundary condition (1.3), as noted in § 1, is that only perturbations aligned with the base flow are produced. This means that no wall-normal velocity component arises, contrary to what would be

expected if the flow were inviscid, and no cross-flow is produced either, even when the wall perturbation has a skewed shape. Nonetheless, both of these features are confirmed by the analysis in the small-roughness limit. In fact, the far field that would be induced by the normal velocity is never produced for any aspect ratio, because its presence is forbidden by mass conservation. Cross-flow exists and can be quantified for a skewed object, but its ratio to the longitudinal velocity tends to zero with decreasing aspect ratio and becomes negligible in the range where linearized boundary conditions apply.

Non-dimensional numerical results for a selection of protuberances and cavities have been plotted in terms of two correction coefficients: a *protrusion* coefficient, accounting for the effect of the aspect ratio, and a *proximity* coefficient, accounting for the interference between equal objects in a periodic array when they are placed at finite distance from each other. The protrusion coefficient for several axisymmetric shapes is fairly close to that of a smoothed cylinder, well approximated by the interpolation formula (8.1). The proximity coefficient is independent of the shape of the object at leading order, and can be determined as a universal function of its non-dimensional volume (volume divided by the period cubed), given by (9.12).

From an application viewpoint, for instance in receptivity calculations like those that are the objective of the European FP7 project 'RECEPT', these results imply that the classical linearized boundary condition (1.3) employed in either already developed or to-be-developed simulation codes can be (i) trusted 'as is' if the aspect ratio of protuberances (or cavities) is within the acceptable range (e.g. ± 0.02 for an error of 10 %), or (ii) replaced by (4.3) if the aspect ratio is larger but irregularities are sparse, or (iii) further multiplied by the proximity coefficient of (9.12) if interaction between irregularities becomes important.

Acknowledgement

Appendix. Variational properties of the asymptotic Stokes problem

In a compact domain Ω, the solution of the Stokes problem minimizes the dissipation

$$D = \frac{1}{4} \int_{\Omega} \left(\frac{\partial v_i}{\partial x_j} + \frac{\partial v_j}{\partial x_i} \right) \left(\frac{\partial v_i}{\partial x_j} + \frac{\partial v_j}{\partial x_i} \right) \mathrm{d}\Omega \tag{A 1}$$

under the constraints of the continuity equation (1.5a) and velocity boundary conditions. Indeed, taking the first variation of (A 1) and integrating by parts gives

$$\delta D = \frac{1}{2} \int_{\Omega} \left(\frac{\partial v_i}{\partial x_j} + \frac{\partial v_j}{\partial x_i} \right) \left(\frac{\partial \delta v_i}{\partial x_j} + \frac{\partial \delta v_j}{\partial x_i} \right) \mathrm{d}\Omega$$

$$= \oint_{\partial\Omega} \delta v_i \left(\frac{\partial v_i}{\partial x_j} + \frac{\partial v_j}{\partial x_i} \right) n_j \, \mathrm{d}\partial\Omega - \int_{\Omega} \delta v_i \frac{\partial}{\partial x_j} \left(\frac{\partial v_i}{\partial x_j} + \frac{\partial v_j}{\partial x_i} \right) \mathrm{d}\Omega. \tag{A 2}$$

Inserting the Stokes momentum equation (1.5b) in the second integral and integrating by parts again reduces this expression to

$$\delta D = \oint_{\partial\Omega} \delta v_i \left[\left(\frac{\partial v_i}{\partial x_j} + \frac{\partial v_j}{\partial x_i} \right) n_j - P n_i \right] \mathrm{d}\partial\Omega + \int_{\Omega} P \frac{\partial \delta v_i}{\partial x_i} \mathrm{d}\Omega, \tag{A 3}$$

where the second integral is null because of the continuity equation. Thus

$$\delta D = -\oint_{\partial \Omega} f_i \delta v_i \, d\partial \Omega, \tag{A 4}$$

where $f_i = P n_i - (\partial v_i / \partial x_j + \partial v_j / \partial x_i) n_j$ is the surface force applied on the boundary of the domain. The standard conclusion of this way of reasoning is that if $\delta v_i = 0$ (because velocity is imposed) on the boundary, D is an extremum. However, just as in the classical application of variational principles to other fields of mechanics, there are a number of additional consequences. One is that if D is seen as a function of velocity boundary conditions, f_i can be identified with the variational derivative $-\delta D / \delta v_i$. Another one is that if the integrations by parts leading to (A 4) are repeated on (A 1) itself rather than on its variation, one finds

$$D = -\frac{1}{2} \oint_{\partial \Omega} f_i v_i \, d\partial \Omega \tag{A 5}$$

(which may also be seen as an application of Euler's formula for homogeneous functions). A third consequence is that if, more generally, velocity boundary conditions are applied on a part $\partial \Omega_v$ of the boundary and force boundary conditions on another part $\partial \Omega_f$,

$$\delta D = -\int_{\partial \Omega_v} f_i \delta v_i \, d\partial \Omega - \int_{\partial \Omega_f} v_i \delta f_i \, d\partial \Omega. \tag{A 6}$$

Let us now particularize the above relationships to the case of Stokes flow between an arbitrarily shaped solid wall at $x_3 = h(x_1, x_2)$ (with $h(x_1, x_2)$ a periodic function for definiteness, although this assumption could be relaxed) and a plane boundary located at $x_3 = H$ where a constant surface force $f_i(x_1, x_2) = F_i$ is imposed. The zero-velocity boundary condition at the solid wall and the periodic lateral conditions contribute zero to either (A 5) or (A 6); therefore, on taking the constant force out of the integral,

$$D = -\frac{1}{2} F_i \int_{x_3 = H} v_i \, dx_1 \, dx_2, \tag{A 7a}$$

$$\delta D = -\delta F_i \int_{x_3 = H} v_i \, dx_1 \, dx_2. \tag{A 7b}$$

If we now let $H \to \infty$, the asymptotic behaviour of velocity at this boundary is such that $v_i \to -F_i x_3 + v'_{i,\infty}$ (for $i = 1 \ldots 2$), where $v'_{1,\infty}$ and $v'_{2,\infty}$ are the same constants that were named u'_∞ and v'_∞ in §5. It follows that the quantity $D' = D - AF^2 H / 2$ (A being the area of an elemental periodic cell) has a finite limit for $H \to \infty$, and

$$A v'_{i,\infty} = -\frac{\partial D'}{\partial F_i}. \tag{A 8}$$

But $v'_{i,\infty}$ is in turn a linear function of F_j, and the matrix connecting them is

$$\frac{\partial v'_{i,\infty}}{\partial F_j} = -\frac{1}{A} \frac{\partial^2 D'}{\partial F_i \, \partial F_j}, \tag{A 9}$$

a symmetric matrix. This proves that the protrusion-height tensor is always symmetric, as was mentioned in §5.

A second useful variational result can be derived if we recall that the solution of the Stokes problem also minimizes the integral of the squared velocity gradient

$$G = \frac{1}{2} \int_{\Omega} \frac{\partial v_i}{\partial x_j} \frac{\partial v_i}{\partial x_j} \, \mathrm{d}\Omega, \tag{A 10}$$

just as it minimizes the integral of its squared symmetric part (A 1). The derivation goes through as above, the only difference being that the velocity gradient appears in the boundary integral in place of the deformation rate. Although on a solid boundary this quantity would not be the true stress, for the behaviour at infinity of the solution the difference is irrelevant. In particular, formulas similar to (A 7) are also valid with G in place of D.

However, with reference to the square of the velocity gradient, one can observe that whereas the solution of the Stokes equations provides the constrained minimum of G using the continuity equation as a constraint, minimizing (A 10) without this constraint yields three independent Laplace equations for v_1, v_2 and v_3, two of which have the trivial solution $v_2 = v_3 = 0$ when the only inhomogeneous boundary condition is imposed on v_1 (at infinity). Since the constrained minimum of some quantity cannot be lower than its unconstrained minimum, it follows that the protrusion height of the Stokes problem cannot be lower than the protrusion height of the Laplace equation for the same geometry.

REFERENCES

BATCHELOR, G. K. 1970 The stress system in a suspension of force-free particles. *J. Fluid Mech.* **41**, 545–570.

BECHERT, D. W. & BARTENWERFER, M. 1989 The viscous flow on surfaces with longitudinal ribs. *J. Fluid Mech.* **206**, 105–129.

BLAKE, J. R. 1971 A note on the image system for a Stokeslet in a no-slip boundary. *Proc. Camb. Phil. Soc.* **70**, 303–310.

HILL, D. C. 1995 Adjoint systems and their role in the receptivity problem for boundary layers. *J. Fluid Mech.* **292**, 183–204.

JOSEPH, D. D., BAI, R., CHEN, K. P. & RENARDY, Y. Y. 1997 Core-annular flows. *Annu. Rev. Fluid Mech.* **29**, 65–90.

KAMRIN, K., BAZANT, M. & STONE, H. A. 2010 Effective slip boundary conditions for arbitrary periodic surfaces: the surface mobility tensor. *J. Fluid Mech.* **658**, 409–437.

LUCHINI, P., MANZO, F. & POZZI, A. 1991 Resistance of a grooved surface to parallel flow and cross-flow. *J. Fluid Mech.* **228**, 87–109.

POZRIKIDIS, C. 1992 *Boundary Integral and Singularity Methods for Linearized Viscous Flow*. Cambridge University Press.

SARKAR, K. & PROSPERETTI, A. 1995 Effective boundary conditions for the Laplace equation with a rough boundary. *Proc. R. Soc. Lond.* A **451**, 425–452.

SARKAR, K. & PROSPERETTI, A. 1996 Effective boundary conditions for Stokes flow over a rough surface. *J. Fluid Mech.* **316**, 223–240.